Initiation and long-term instability of the East Antarctic Ice Sheet

Sean P. S. Gulick[1], Amelia E. Shevenell[2*], Aleksandr Montelli[1†], Rodrigo Fernandez[1], Catherine Smith[2], Sophie Warny[3], Steven M. Bohaty[4], Charlotte Sjunneskog[5], Amy Leventer[6], Bruce Frederick[1††], Donald D. Blankenship[1]

[1]Institute for Geophysics, Jackson School of Geosciences, University of Texas at Austin, Austin, Texas 78758, USA.

[2]College of Marine Science, University of South Florida, Saint Petersburg, Florida, 33701, USA.

[3]Department of Geology and Geophysics and Museum of Natural Science, Louisiana State University, Baton Rouge, Louisiana, 70803, USA.

[4]School of Ocean and Earth Science, University of Southampton, Southampton S0143ZH, UK.

[5]Antarctic Marine Geological Research Facility, Florida State University, Tallahassee, Florida, 32306, USA.

[6]Geology Department, Colgate University, Hamilton, New York, 13346, USA.

*Joint first-author.
†Present Address: Scott Polar Research Institute, University of Cambridge, Cambridge, CB2 1ER, UK.
††Present Address: Department of Geology, University of Kansas, Lawrence, Kansas, 66045, USA.

Continental-scale Antarctic ice sheets have evolved over the last 50 million years[1-4]. However, sparse ice-proximal records[5-8] limit understanding of past East Antarctic Ice Sheet (EAIS) behavior and thus, our ability to evaluate its response to ongoing environmental change. The EAIS is marine-based within the Aurora Subglacial Basin (ASB), indicating that this catchment, which drains ice to the Sabrina Coast, may be sensitive to climate perturbations[9-11]. Here we show, using marine geological and geophysical data from the continental shelf seaward of the ASB, that marine-terminating glaciers existed at the Sabrina Coast by the early-to-middle Eocene. This finding implies substantial ice volume in the ASB before continental-scale marine-terminating ice sheets were established ~34 million years ago[1-4]. Subsequently, ice advanced and retreated from the ASB and across the continental shelf at least eleven times during the Oligocene and Miocene. Tunnel valleys[12] associated with half of these glaciations indicate a surface meltwater-rich sub-polar glacial system existed under climate conditions similar to those anticipated with continued anthropogenic warming[10,11]. Cooling since the Late Miocene[13] resulted in an expanded polar EAIS and a limited ASB catchment response to Pliocene warmth[14-16]. Geologic records indicate that atmospheric temperature and surface-derived meltwater may play important roles in Antarctic ice mass balance under warmer than present climates, with significant implications for future global sea level projections[10,11,15,17].

The East Antarctic Ice Sheet (EAIS) response to anthropogenic warming and contribution to global sea level are the largest uncertainties in climate models because EAIS formation, evolution, and behavior during past warm climates are poorly understood[10,11]. Deep-sea benthic foraminifer oxygen isotopes ($\delta^{18}O$) indicate that during the early Eocene (53-51 million years ago (Ma)), Earth experienced the warmest conditions of the past 65 million years (myr)[1,4,17,18]. This warmth was followed by ~15 myr of cooling, declining atmospheric CO_2, tectonic reorganizations, and development of continental-scale Antarctic ice sheets by the earliest Oligocene (33.6 Ma)[1-4,17-19]. As atmospheric CO_2

declined through the Oligocene and Miocene, deep-sea $\delta^{18}O$ and far-field sea level records suggest that ice sheets advanced to and retreated from Antarctica's continental shelves in response to astronomically-paced changes in solar insolation[3,4,18,20,21]. These records also suggest larger Antarctic ice sheets with less pronounced growth and decay cycles after the middle Miocene (~13.8 Ma)[1,4], when global climate was cool and atmospheric CO_2 concentrations low, relative to the Eocene and Oligocene[4,17]. While far-field records provide a general framework for understanding Cenozoic Antarctic cryosphere development, these records provide little direct evidence for ice location, extent, or thermal conditions required to assess climate forcings and feedbacks involved in Antarctic cryosphere and global climate evolution and are complicated by Northern Hemisphere ice volume in the Plio-Pleistocene[1,3,4].

East Antarctic continental margin and the Southern Ocean sediments provide direct evidence of EAIS evolution, indicating regional marine-terminating ice in the late Eocene[22-24] and astronomically-paced glacial-interglacial cycles through the Pliocene[5,6,14]. However, existing ice-proximal records are geographically limited and temporally discontinuous, making regional comparisons difficult. Recent ice sheet models provide additional insight into EAIS evolution[10,11,25]. Outputs indicate that EAIS catchments with deep landward-dipping subglacial topography and surface meltwater, including the Aurora Subglacial Basin (ASB), may be sensitive to climate perturbations (e.g. atmospheric and/or oceanic temperatures, atmospheric CO_2, sea level)[9-11,25]. However, outputs depend on poorly constrained initial boundary conditions[17,24,25], feedbacks[18], and retreat mechanisms[11]. Thus, significant uncertainties remain regarding EAIS evolution

74 that can only be resolved with well-dated ice-proximal marine geologic and geophysical
75 data[1,19].
76
77 To improve predictions of future EAIS response to warming and contribution to global
78 sea level rise[10,11], knowledge of EAIS evolution in catchments with large potential sea-
79 level contributions is critical. The low-lying glacially sculpted ASB catchment (~3-5 m
80 sea-level equivalent ice[9,15,26]; Fig. 1a) drains ice from the Gamburtsev Mountains to the
81 Sabrina Coast via the Totten Glacier, which is experiencing the largest mass loss in East
82 Antarctica[27] and is influenced by warm subsurface (deeper than 400 m) ocean waters at
83 its grounding line[28]. The ASB catchment consists of several over-deepened basins[15,26] and
84 hosts an active subglacial hydrological system that drains basal meltwater to the ocean[29],
85 suggesting that regional outlet glaciers may be susceptible to both progressive retreat[13]
86 and changing subglacial hydrology[29]. Thus, regional glacial dynamics and, ultimately, sea
87 level contribution during a given warm interval depends on both catchment and glacier
88 boundary conditions (e.g., subglacial topography, substrate, and/or meltwater
89 presence/volume) coupled to atmospheric and oceanic forcings.
90
91 We present the first ice-proximal marine geophysical and geological records of ASB
92 glacial evolution (Methods; Figs. 1b, 2, 3a). To document regional glacial development,
93 ice dynamics, and the timing of significant environmental transitions, we integrate
94 seismic reflection and sedimentary data from the Sabrina Coast continental shelf, at the
95 outlet of the ASB (Fig. 1b). This margin formed during Late Cretaceous rifting of
96 Antarctica and Australia, with tectonic subsidence continuing through the Paleogene[8].

97 The present-day continental shelf is ~200 km wide, ~600 m deep, and slopes landward
98 (Fig. 1b). We imaged ~1300 m of dipping sedimentary strata that overlie acoustic
99 basement on the inner continental shelf (Methods; Fig. 1b). We identified three distinct
100 packages of sedimentary rocks bounded by basement, regionally extensive
101 unconformities, and the seafloor, termed Megasequences I-III (MS-I, -II, -III; Figs. 2a,
102 2c, 3a, Extended Data Fig. 1). Glacial erosion truncated imaged reflectors at the sea floor,
103 allowing us to recover and date strata near the top of MS-I and at the base of MS-III
104 (Methods; Figs. 2a, 2c).
105
106 The deepest unit, MS-I, overlies basement and consists of a ~620 m thick, seaward
107 dipping sequence of low-amplitude discontinuous reflectors that increase in amplitude
108 and lateral continuity up-section (Methods; Fig. 2a, Extended Data Fig. 1). No evidence
109 of glacial erosion exists within these strata (Figs. 2a, 3a, Extended Data Fig. 1). On the
110 mid-shelf, we imaged two intervals of inclined stratal surfaces (clinoforms), indicating
111 times of high sediment flux to an unglaciated continental margin (Fig. 2a). Piston core
112 NPB14-02 JPC-55 (1.69 m) recovered mica-rich silty sands 15-20 m below the upper
113 clinoform (Methods; Fig. 2a, Extended Data Figs. 1b, 2a, Extended Data Table 1).
114 Terrestrial palynomorphs and benthic foraminifers indicate that these marine sediments
115 are late Paleocene in age (Methods; Fig. 2b, Extended Data Figs. 1, 2, 5, Extended Data
116 Tables 2, 3), confirming the pre-glacial seismic interpretation of MS-I.
117
118 Above the upper clinoform, within MS-I, are a series of moderate- to high-amplitude,
119 laterally variable reflectors (gray shading; Methods; Fig. 2a, Extended Data Fig. 1).

120 Piston core NBP14-02 JPC-54 (1.2 m; Methods; Fig. 2a, Extended Data Figs. 1b, 3),
121 recovered from this interval, contains centimeter-scale lonestones interpreted as ice-rafted
122 debris (IRD). Terrestrial palynomorphs indicate that these sediments are of early-to-
123 middle Eocene age (Methods; Fig. 2b, Extended Data Table 2). Laterally variable
124 reflectivity without chaotic seismic facies, with IRD, and no evidence for cross-shelf
125 glacial erosion indicate that marine-terminating glaciers were present at the Sabrina Coast
126 by the middle Eocene, but grounded ice had not yet advanced across the shelf (Figs. 2a,
127 3a).
128
129 MS-I strata reveal episodes of enhanced sediment flux from the ASB, followed by the
130 early-to-middle Eocene arrival of marine-terminating glaciers to the Sabrina Coast.
131 Models and observations indicate that Antarctica's ice sheets nucleated in the higher
132 elevations of the Gamburtsev Mountains and first reached the ocean near the Sabrina
133 Coast and Prydz Bay[19], increasing sediment flux to the Australo-Antarctic Gulf[30]. Within
134 the ASB are a series of topographically constrained basins that likely hosted
135 progressively larger ice volumes[15,26] as ice expanded in the catchment (Fig. 1a). We
136 speculate that after the early Eocene climate optimum (53-51 Ma), as regional and global
137 temperatures cooled and atmospheric CO_2 declined[17,18] (Figs. 3b-c), glacial ice breached
138 the northern ASB highlands[26], allowing marine-terminating glaciers to deliver IRD to the
139 Sabrina Coast shelf by the early-to-middle Eocene (Figs. 1a, 2a, Extended Data Fig. 2).
140 This finding is significant and indicates 1) substantial East Antarctic ice volume by the
141 early-to-middle Eocene and 2) the relatively early arrival of marine-terminating glaciers
142 to the Sabrina Coast, compared with late Eocene arrivals in Prydz Bay and the Weddell

143 Sea[22-24]. Due to the relative paucity of Eocene data from Antarctica's margins, it is not
144 clear if this early arrival is unique to the Sabrina Coast, or if equivalent data have not yet
145 been recovered.
146
147 Up-section (~13 m) from core JPC-54, the deepest regionally mappable roughly-eroded
148 surface (dark blue horizon; Figs. 2a, 3a, Extended Data Fig. 1) separates MS-I from MS-
149 II strata and provides the first preserved evidence of grounded ice on the Sabrina Coast
150 shelf (Methods). MS-II is up to 675 m thick with ten additional erosive surfaces (gray
151 numbered horizons; Fig. 3a, ED Fig. 1) that truncate reflectors and exhibit rough
152 morphology and/or channels indicative of glacial erosion in a meltwater-rich
153 environment[7,12,29,30] (Methods). Between erosive surfaces, we observe strata with parallel
154 high-amplitude reflectivity and prograding strata of varying thickness (Methods), which
155 indicate open marine conditions and intervals of high sediment flux[7,8], respectively,
156 between the 11 glacial advances and retreats from the ASB.
157
158 Unlike previously imaged East Antarctic shelf sequences[7,8], Sabrina Coast MS-II reveals
159 multiple erosive surfaces (2-6, 8, 9) with U-shaped channels carved into sedimentary
160 strata (Fig. 3a). Based upon geometry and size (Methods; ≤170 m deep; ~1150 m wide),
161 these channels are consistent with subglacial tunnel valleys observed in surface
162 meltwater-rich sub-polar glacial systems[12]. The most significant channels are associated
163 with surfaces 3-5, 8, and 9 (Fig. 3a, Extended Data Fig. 1e). Overlying erosive surface 11
164 (Fig. 3a, Extended Data Fig. 1e) is a ~330 m thick sequence of seaward dipping strata
165 devoid of rough erosional surfaces, indicating prolonged continental shelf progradation

and/or high sediment flux in an open marine setting[7,8]. A regional landward-dipping angular unconformity truncates seaward-dipping MS-II (and in some places, MS-I) strata (light blue horizon; Figs. 2a, 2c, 3a, Extended Data Fig. 1). Late Miocene-to-earliest Pliocene diatomites were recovered from and immediately above the unconformity (Figs. 2c-d, Extended Data Figs. 1, 4, 6). As we may not have recovered sediments below the unconformity, we consider the late Miocene (~7-5.5 Ma) the youngest possible age for the MS-III base (Fig. 2d).

Ice advanced across the Sabrina Coast continental shelf at least 11 times from the early-to-middle Eocene to late Miocene (Fig. 3a), when average atmospheric CO_2 concentrations (Fig. 3b), global temperatures (Fig. 3c), and global sea levels (Fig. 3d) were similar to or higher than present[4,17,18]. Without additional age constraints, the pacing of these glaciations is unknown, but far-field and ice-proximal records indicate cryosphere sensitivity to astronomically-paced insolation changes during the Oligo-Miocene[5,20,21]. The scale of Sabrina Coast shelf tunnel valleys and the presence of similar channels within the ASB catchment, ~400 km from the present grounding line, suggest that regional subglacial hydrologic systems were fed by large volumes of surface meltwater during Oligo-Miocene glacial-interglacial cycles (Methods)[11,15]. Thus, during climates similar to or warmer than present, surface-derived meltwater may play an important role in EAIS behavior[29], as indicated by models[11]. The prograding sequence at the top of MS-II is similar to middle to late Miocene sequences in Wilkes Land and Prydz Bay, which reflect the transition from sub-polar to polar glacial regimes[7,8] (Fig. 3a, Extended Data Fig. 1e).

Above the regional unconformity, MS-III consists of a ≤110 veneer of sub-horizontal to landward-dipping strata that thicken landward, indicating substantial glacial erosion of MS-II and/or lower regional sediment flux and onset of ice loading by the late Miocene[8] (Methods; Figs. 2a, 2c, 3a, Extended Data Fig. 1). MS-III strata contain no visible channels, suggesting reduced regional surface meltwater influence and/or more diffuse basal meltwater flux[12,15,26,29]. High-amplitude reflectors (Fig. 3a) within acoustically chaotic MS-III strata indicate erosional surfaces in late Miocene to Pleistocene tills (Methods) and advance/retreat of an expanded EAIS[15]. Open marine sediments are present, but the lack of significant accumulation and/or preservation suggests limited regional ice retreat and/or shorter interglacials since the late Miocene (Methods; Figs. 2c, 3a, Extended Data Fig. 1).

An expanded polar EAIS occupied the ASB catchment and Sabrina Coast continental shelf since the late Miocene[15], coincident with significant global climate ,carbon and hydrologic cycle reorganizations[4,13], continent-wide ice sheet expansion and stabilization[7,8,13], Antarctic Circumpolar Current intensification, Southern Ocean cooling, and modern meridional thermal gradient development (Fig. 3b)[1,13]. Atmospheric cooling likely limited the amount of regional surface ablation, resulting in ice expansion and reduced surface-derived meltwater in the ASB catchment. Although open marine conditions intermittently existed on the shelf, the relative MS-III thickness and patterns of erosion within the ASB catchment suggest maximum grounding line retreat of ~150 kilometers[15] from its present location since the late Miocene. Thus, in contrast to the

adjacent Wilkes Subglacial Basin[14], the ASB did not contribute significantly to sea level rise during Pliocene warmth[15,16].

Sabrina Coast shelf records reveal the importance of atmospheric temperatures and surface-derived meltwater to Antarctica's ice mass balance. Although deeper, more continuous sampling of these sediments is required to assess the timing, magnitude, and rates of EAIS evolution in the ASB, the ice-proximal Sabrina Coast shelf record confirms model predictions of the region's long-term sensitivity to climate[10,11,15,25,26]. Critical for future global sea level rise scenarios is the potential for ASB catchment glaciers to revert from the extensive polar system of the last ~7 Ma to the surface meltwater-rich sub-polar system of the Oligo-Miocene (Fig. 3a), when average global temperatures and atmospheric CO_2 concentrations were similar to those anticipated under current warming projections (Figs. 3b-c)[10,11,17]. Presently, the Totten Glacier is thinning faster than any other East Antarctic outlet glacier[11,27,28] due to ocean thermal forcing[28]. Our findings suggest that ice in the ASB catchment may respond dramatically to anthropogenic climate forcing if regional atmospheric warming results in surface meltwater production.

References

1. Kennett J.P. Cenozoic evolution of Antarctic glaciation, the circum-Antarctic ocean, and their impact on global paleoceanography. *J. Geophys. Res.* **82**, 3843-3860 (1977).

2. Coxall, H.K. et al. 2005. Rapid stepwise onset of Antarctic glaciation and deeper calcite compensation in the Pacific Ocean. *Nature* **433**, 53-57 (2005).

3. Kominz, M.A., Browning, J.V., Miller, K.G., Sugarman, P.J., Mizintseva, S. & Scotese, C.R. Late Cretaceous to Miocene sea-level estimates from the New Jersey and Delaware coastal plain coreholes: An error analysis. *Basin Research*

20, 211-226 (2008).

4. Mudelsee, M., Bickert, T., Lear, C.H. & Lohmann, G. Cenozoic climate changes: A review based on time series analysis of marine benthic $\delta^{18}O$ records. *Rev. Geophys*. **52**, 333-374 (2014).

5. Naish, T.R. *et al.* Orbitally induced oscillations in the East Antarctic ice sheet at the Oligocene/Miocene boundary. *Nature* **413**, 719-723 (2001).

6. Naish, T.R. *et al.* Obliquity-paced Pliocene West Antarctic ice sheet oscillations. *Nature* **458**, 322-328 (2009).

7. Cooper, A.K. *et al*. Cenozoic climate history from seismic reflection and drilling studies on the Antarctic Continental Margin. *In*: Florindo, F., Siegert, M. (Eds.), Antarctic Climate Evolution. *Developments in Earth and Environmental Sciences*. Elsevier, pp. 115-228 (2009).

8. Escutia, C., Brinkhuis, H., Klaus, A. & Expedition 318 Scientists. Proc. Integrated Ocean Drilling Program 318 (Ocean Drilling Program Management International, Tokyo) (2011).

9. Fretwell, P. *et al*. Bedmap2: improved ice bed, surface and thickness datasets for Antarctica. *Cryosphere* **7**, 375-393 (2013).

10. Golledge, N.R. *et al*. The multi-millennial Antarctic commitment to future sea-level rise. *Nature* **526**, 421-425, (2015).

11. DeConto, R.M. & Pollard, D. Contribution of Antarctica to past and future sea-level rise. *Nature* **531**, 591-597 (2016).

12. Kehew, A.E., Piotrowski, J.A. & Jørgensen, F. Tunnel valleys: Concepts and controversies – A review. *Earth-Sci. Rev.* **113**, 33-58 (2012).

13. Herbert, T.D. *et al.* Late Miocene global cooling and the rise of modern ecosystems. *Nat. Geosci.* **9**, 843-847 (2016).

14. Cook, C.P. *et al.* Dynamic behavior of the East Antarctic ice sheet during Pliocene warmth. *Nat. Geosci.* **6**, 765-769 (2013).

15. Aitken, A.R.A. *et al*. Repeated large-scale retreat and advance of Totten Glacier indicated by inland bed erosion. *Nature* **533**, 385-389 (2016).

16. Rovere, A. *et al*. The Mid-Pliocene sea-level conundrum: Glacial isostasy, eustacy, and dynamic topography. *Earth Planet. Sci. Lett.* **387**, 27-33 (2014).

17. Masson-Delmotte V. *et al*. Information from paleoclimate archives. *In* Climate

Change 2013: The Physical Science Basis. Contribution of Working Group I to the Fifth Assessment Report of the Intergovernmental Panel on Climate Change (T.F. Stocker *et al.* (eds.), pp. 383–464. Cambridge, UK: Cambridge University Press (2013).

18. Anagnostou, E. *et al.* Changing atmospheric CO_2 concentration was the primary driver of early Cenozoic climate. *Nature* **533**, 380-384 (2016).

19. DeConto, R.M. & Pollard, D. Rapid Cenozoic glaciation of Antarctica induced by declining atmospheric CO_2. *Nature* **421**, 245-249 (2003).

20. Pälike H. *et al*. The heartbeat of the Oligocene climate system. *Science* **314**, 1894-1898 (2006).

21. Liebrand, D. *et al.* Evolution of the early Antarctic ice ages. *Proc. Natl. Acad. Sci. USA* **114**, 3867-3872 (2017).

22. Scher, H.D., Bohaty, S.M., Smith, B.W. & Munn, G.H. Isotopic interrogation of a suspected late Eocene glaciation. *Paleoceanography* **29**, 628-644 (2014).

23. Carter, A., Riley, T.R., Hillenbrand, C-D. & Rittner, M. Widespread Antarctic glaciation during the late Eocene. *Earth Planet. Sci. Lett.* **458**, 49-57 (2017).

24. Passchier, S., Ciarletta, D.J., Miriagos, T.E., Bijl, P.K. & Bohaty, S.M. An Antarctic stratigraphic record of stepwise ice growth through the Eocene-Oligocene transition. *GSA Bull*. **129**, 318-330 (2017).

25. Golledge, N.R., Levy, R.H., McKay, R.M., & Naish, T.R. East Antarctic ice sheet most vulnerable to Weddell Sea warming. *Geophys. Res. Lett.* **44**, 2343-2351 (2017).

26. Young, D.A. *et al*. A dynamic early East Antarctic Ice Sheet suggested by ice-covered fjord landscapes. *Nature* **474**, 72-75 (2011).

27. Li, X., Rignot, E., Mouginot, J., & Scheuchl, B. Ice flow dynamics and mass loss of Totten Glacier, East Antarctica, from 1989 to 2015. *Geophys. Res. Lett.* **43**, 6366–6373 (2016).

28. Rintoul, S.R. *et al.* Ocean heat drives rapid basal melt of the Totten Ice Shelf. *Sci. Adv.* **2**, e1601610 (2016).

29. Wright, A.P. *et al.* Evidence of a hydrological connection between the ice divide and ice sheet margin in the Aurora Subglacial Basin, East Antarctica. *J. Geophys. Res.* **117**, F01033, doi: 10.1029/2011JF002066 (2012).

30. Close, D.I., Stagg, H.M.J & O'Brien, P.E. Seismic stratigraphy and sediment

distribution on the Wilkes Land and Terre Adélie margins, East Antarctica. *Mar. Geol.* **239**, 33-57 (2007).

Supplementary Information is available in the online version of this paper.

Acknowledgements We thank the NBP14-02 science party, ECO captain and crew, and ASC technical staff aboard the *RV/IB N.B. Palmer*. NBP14-02 was supported by the National Science Foundation (NSF PLR-1143836, -1143837, -1143843, -1430550, and -1048343) and a GSA graduate student research grant to C. Smith. We thank the Antarctic Marine Geology Research Facility staff at Florida State University for sampling assistance and E. Thomas, M. Katz, F. Sangiorni, P. Bijl, and S. Manchester for discussions. This is UTIG Contribution #3137.

Author Contributions S.G. and A.S. contributed equally to this work, co-writing the manuscript with input from all authors. D.B., S.G., A.L., and A.S. conceived the study. B.F, R.F., S.G., A.L., A.S., C.S., and the shipboard scientific party collected geophysical data and samples on USAP cruise NBP14-02. All authors contributed to the analyses and interpretation of the results.

Author Information Reprints and permissions information is available at www.nature.com/reprints. The authors declare no competing financial interests. Readers are welcome to comment on the online version of the paper. Correspondence and requests for materials should be addressed to S.G. (sean@ig.utexas.edu).

Figure Captions

Figure 1| Aurora Subglacial Basin elevations and Sabrina Coast bathymetry. a, Aurora Subglacial Basin (ASB) elevations[9] and Sabrina Coast shelf study location (black box; NBP14-02 (yellow) and published (white)[30] seismic lines indicated). Inset: ASB location (black box), Antarctica. ASB highlands (brown), reduced ice glacial pathways (white arrows)[26], approximate retreated Oligo-Miocene (solid line) and late Miocene-Pleistocene (dashed line) grounding line locations[15]. **b**, NBP14-02 seismics, bathymetry, and BEDMAP2 bathymetry[9]; interpreted seismic lines (red) and jumbo piston cores (JPC; white) indicated. Inset: Regional bathymetry[9] and seismics. Sabrina Coast coastline, Moscow University Ice Shelf (MUIS), and shelf break indicated.

Figure 2| Sabrina Coast seismic and piston core biostratigraphy. a, Seismic line 17 with cores in Megasequence I (MS-I, pre- to pro-glacial (gray shading)). MS-II (meltwater-rich glacial) overlies first expression of grounded ice (dark blue horizon). MS-III (glacial) overlies regional unconformity (light blue horizon). **b**, Biostratigraphy for JPC-55, based on pollen and benthic foraminifers (late Paleocene; brown shading), and JPC-54, based on pollen (early-to-middle Eocene; beige shading). **c**, Seismic line 13 with cores relative to regional unconformity (light blue horizon). **d**, JPC-30 and -31 diatom biostratigraphy, with conservative (beige shading, red line) and preferred (brown shading, blue line) ages.

Figure 3| Composite Sabrina Coast section with glacial surfaces and climate indicators. a, Composite seismic line with pre- to pro-glacial Megasequence I (MS-I;

black), glacial MS-II with erosion surfaces (initial: dark blue; subsequent: gray) overlain by a non-glacial interval and regional unconformity (light blue), and polar glacial MS-III. **b**, Cenozoic atmospheric CO_2 reconstructions[17,18] with 2 standard deviation error bars (black). **c**, Composite high-latitude benthic formainifer $\delta^{18}O$ record with blue uncertainty band generated/calculated as per [4], reflecting global ice volume and deep ocean temperatures[4]; **d**, New Jersey margin sea-level lowstands (black) with minimum uncertainty (grey envelope) and best estimates (blue line)[3].

METHODS

Seismic Data Acquisition, Processing, and Interpretation

The 750 km of 3-m resolution multichannel seismic data were acquired using dual 45 in^3 generator-injector (GI) guns and a 75-m long, 24-channel streamer in 2014 in heavy ice conditions aboard the *RV/IB N. B. Palmer*. Data processing followed standard steps of filtering, spherical divergence correction, normal moveout correction, and muting, but no deconvolution was required due to the quality of the GI source. All sediment thicknesses are presented in meters and based on a velocity of 2250 m/s; seafloor depths are based on a velocity of 1500 m/s. Acoustic basement is the limit of our reflectivity and interpreted as crystalline rock.

Seismic megasequences were identified based upon the presence or absence of erosional surfaces and seismic facies of the mappable units within the sediment packages. Seismic facies observed include: 1) stratified (laminated) or semi-stratified intervals interpreted as open marine, 2) relatively continuous layers with variable reflectivity interpreted as open marine conditions influenced by ice-rafting, and 3) chaotic,

403 discontinuous or transparent intervals interpreted as glacial to periglacial conditions. MS-
404 I exhibits stratified, semi-stratified, and variably reflective (grey shading) intervals. MS-
405 II exhibits chaotic and discontinuous intervals related to erosive surfaces, stratified or
406 semi-stratified intervals, and prograding intervals. Rough, undulatory surfaces are
407 indicators of glacial advance on continental shelves[31]. MS-III consists of chaotic or
408 acoustically transparent intervals with thin intervals of stratified facies. The thickness of
409 stratified intervals between erosional surfaces may be a proxy for duration of open water
410 conditions and/or extent of ice retreat (and thus time/distance for readvance)[32]. Thus, MS-
411 II includes extensive and/or long-lasting glacial retreats whereas MS-III records localized
412 or relatively short-lived retreats.

413 All identified horizons are regionally mappable within the seismic survey area.
414 Glacial erosion surfaces are interpreted based on roughness, extent of down-cutting, and
415 association with overlying chaotic or discontinuous facies. Tunnel valley determinations
416 are based on comparisons with imaged tunnel valleys from the North Sea, Alaska, and
417 Svalbard[32-38]. Hydrologic modeling suggests tunnel valleys only form when meltwater
418 exceeds the capacity of flow through porous glacial substrate and any sheet flow at the
419 base of a glacier[39]. As tunnel valley size is expected to relate to discharge of subglacial
420 meltwater, Sabrina Coast glacial erosion surfaces 3-5 and 8-9 are interpreted as
421 meltwater-rich glaciations that likely required surface-derived meltwater. In the Ross Sea,
422 a widespread regional unconformity that separates prograding shelf strata from glacial
423 tills was interpreted to indicate widespread ice sheet expansion and the onset of ice
424 loading, as suggested for the Sabrina Coast angular unconformity underlying MS-III[40].
425 Uninterpreted versions of the seismic profiles in Figs. 2a, c and 3a, including individual

lines from the regionally representative cross-shelf composite line (Fig. 3a), are included as Extended Data (Extended Data Fig. 1).

Marine sediment collection, description, and physical properties analyses

Marine sediments were collected in 440 to 550 meters of water 100-150 km offshore, on the Sabrina Coast continental shelf (Extended Data Table 1). Geophysical data guided the recovery of a suite of four <2 m long jumbo piston cores (JPCs) that targeted outcropping reflectors on the continental shelf (Figs. 1b, 2a, 2c, Extended Data Figs. 2-4). Seismic data, lithology, benthic foraminifers, diatoms, and bulk sediment geochemistry confirm that these sequences were deposited in open marine to subglacial settings. Sediment cores were transported (unsplit and at 4°C) to the Antarctic Marine Geological Research Facility at Florida State University, where they were split, photographed, visually described, x-rayed, and GEOTEK Multi-sensor Core Logger (MSCL) data were collected following standard protocols. The radiographs were interpreted in Adobe Photoshop with the contrast adjusted for each image. Organic carbon, $\delta^{13}C$, and $\delta^{15}N$ analyses of bulk sediments were conducted using a Carlo Erba 2500 Elemental Analyzer coupled to a continuous flow ThermoFinigan Delta Plus XL IRMS at USF CMS following standard methods. Lithologic, physical properties, and geochemical data are shown in Extended Data Figures 2-4 and provided in Supplementary Information (SI).

Core JPC-55 (1.69 m) contains two distinct lithologic units (Extended Data Fig. 2b). The upper unit (0-0.4 m; Unit 1) consists of Quaternary-recent diatom-rich sandy silt with relatively high magnetic susceptibility (SI) overlying a more consolidated lower unit

449 (0.4-1.69 m; Unit 2) of homogenous black micaceous silty fine sands with organic
450 detritus, rare pyrite nodules, macro- and microfossils, and a ~10 cm diameter spherical
451 siderite concretion nucleated around a monocot stem (Extended Data Figs. 2b, d, e; SI).
452 Core JPC-54 (1.21m), collected above the youngest clinoform, contains two
453 distinct lithologic units (Fig. 2a, Extended Data Fig. 3b). The lithology of the upper unit
454 (0-0.2 m; Unit 1) in JPC-54 is similar to that of JPC-55 and overlies a lower unit (0.2-
455 1.21 m; Unit 2) composed of structureless gravel-rich sandy silts to silty coarse sands
456 with centimeter-scale angular lonestones throughout Units 1 and 2 (Extended Data Fig.
457 3b). A conservative approach to ice-rafted debris (IRD) interpretation was undertaken in
458 these sediments and only angular lonestones ≥1 cm were interpreted as IRD. Lighter
459 colored sediment with modern diatoms, visible on the right-hand side of JPC-54,
460 indicates flow-in below ~80 cm, likely due to a partial piston stroke; flowage of dark
461 sediment along the right side of the upper core is consistent with this interpretation and/or
462 on-deck or transport disturbance (Extended Data Fig. 3b). However, angular lonestones
463 are observed throughout and a majority are surrounded by the dark colored sediments.
464 Core JPC-30 (0.52 m plus cutter nose) contains diatom-bearing sandy muds, with
465 intervals of well-sorted sands (0-0.25 m). Sub-angular diatomite clasts are present in a
466 mud matrix between 0.25 and 0.52 m. In the core cutter nose, we recovered stratified
467 diatomite and gravelly diatom-bearing sandstone and sandy diatomite above a sharp
468 contact with sandy diamictite below (Extended Data Fig. 4b).
469 Core JPC-31 (0.47 m) contains an upper unit of muddy diamicton (0-0.29 m).
470 Between 0.29 and 0.47 m, angular diatomite clasts are present, which may have been
471 fractured during coring (Extended Data Fig. 4c).

472

473 **Biostratigraphic methods**

474 *Palynology:* Nine samples from JPC-54 and eight samples from JPC-55
475 (Extended Data Figs. 2b, 3b, Extended Data Table 2) were processed at Global Geolab
476 Limited, Alberta, Canada using palynological techniques suited for Antarctic sediments.
477 Approximately five grams of dried sediment were weighed and spiked with a known
478 quantity of *Lycopodium* spores to allow computation of palynomorph concentrations.
479 Acid soluble minerals (carbonates and silicates) were removed via digestion in HCl and
480 HF acids. Residues were concentrated by filtration through a 10-µm sieve and mounted
481 on microscope slides for analyses. Analysis was conducted under 100x oil immersion
482 objective with a Zeiss Axio microscope. For samples with sufficient palynomorph
483 abundance, a minimum of 300 palynomorphs were tabulated per sample. For samples
484 with low abundance, the entire residue was tabulated. A database of all palynomorphs
485 recovered was prepared and key species were photographically documented. The
486 taxonomic evaluation was completed based on the type specimen repository and library at
487 the Louisiana State University Center for Excellence in Palynology (CENEX).
488 Palynological results are presented in Extended Data Table 2.

489 *Benthic Foraminifera:* Benthic foraminifer counts and biostratigraphic data were
490 generated for 16 depths in JPC-55 and five depths in JPC-54 using standard protocols
491 (Extended Data Figs. 2b, 5, Extended Data Table 3). Sediment samples between 20 and
492 30cc were washed over a 63-µm sieve with deionized water. Sample residues were dried
493 at 50°C for 24 hours, transferred to labeled vials, dry sieved into 250- and 150-µm
494 fractions, and examined using a Zeiss Stemi 2000-C stereomicroscope with a 1.6X lens

and 10X eyepiece (Magnification: 10.4-80X). Genus and species identifications were refined using Scanning Electron Microscopy (SEM) at the University of South Florida College of Marine Science (Extended Data Fig. 5). All benthic foraminifer individuals present in each JPC-55 sample are tabulated in Extended Data Table 3. In JPC-55, preservation of aragonite and calcium carbonate tests, determined both visually and via SEM, ranges from poor to excellent (Extended Data Fig. 5). Five species of well-preserved aragonitic and calcareous benthic foraminifers were observed throughout JPC-55 Unit 2 (ED Table 3). No foraminifers were observed in JPC-54.

Diatoms: Diatom biostratigraphy was conducted on two sets of NBP14-02 samples: 1) JPC-30 cutter nose diatomites and 2) diatomite clasts from the bottom of JPC-31 (Extended Data Figs. 4b, 4d, 6). Quantitative slides were prepared at Colgate University for diatom assemblage studies and biostratigraphic evaluation using a settling technique that results in a random and even distribution of frustules[41]; sub-samples were sieved at 10- and 63-μm to concentrate unbroken frustules for examination. Photographic documentation at 1000x magnification using oil immersion on Olympus BX50 and BX60 microscopes was completed at Colgate University (Extended Data Fig. 6). The beige shading in Fig. 2d represents the conservative zonal assignment and age range, whereas the brown shading represents the refined age interpretation. Age constraints for key diatom bioevents are derived from the statistical compilation and analysis of average age ranges for Southern Ocean taxa[42.]

Chronology

517 *Palynological biostratigraphic zonation scheme:* Palynological biostratigraphic
518 zonation of cores NBP14-02 JPC-54 and JPC-55 is based on the presence of a few key
519 species and limited data available from Antarctica and surrounding regions (e.g. Australia
520 and New Zealand). *Gambierina edwardsii* and *Gambierina rudata* are known as
521 Cretaceous to Paleocene species. A recent study published a robust LAD for these species
522 at the Paleocene/Eocene boundary on the East Tasman Rise (ODP Site 1172)[43]. However,
523 in southeastern Australia, the two *Gambierina* species observed in the Sabrina Coast
524 sequence range into the earliest early Eocene[44]. Extended ranges for the *Gambierina* sp.
525 (dashed lines; Fig. 2b) are based on the palynological analysis of ODP Site 1166 in Prydz
526 Bay[45,46], where abundant well-preserved *Gambierina* specimens were observed and not
527 considered reworked. Consequently, those authors extended the *Gambierina* sp. range
528 into the early-to-middle Eocene in East Antarctica[45,46].
529 *Microalatidites paleogenicus* has a Paleogene to Neogene range[46]. Although we
530 are adopting their range herein, there is some controversy with this range. The first
531 occurrence of *Microalatidites paleogenicus* is listed as Senonian in Australia and New
532 Zealand[47], but there is no robust evidence supporting an extended range in Antarctica. In
533 Fossilworks (PaleoDB taxon number: 321781), *Microalatidites paleogenicus* is listed as
534 having a range from 55.8 to 11.608 Ma.
535 *Nothofagidites lachlaniae* ranges from Paleogene to modern while *Nothofagidites*
536 *flemingii-rocaensis* ranges from Paleogene to Neogene[46]. The range for *N. lachlaniae* in
537 New Zealand is listed as Late Cretaceous to present and is similar to other forms[48]. In the
538 Paleocene and Eocene, there is climatically-induced variability observed in the
539 *Nothofagidites* ranges. For example, broad regional vegetation changes (e.g. the

abundance of *Nothofagidites lachlaniae* in western Southland (Ohai, Waiau and Balleny basins) and its scarcity in other Eocene sections (Waikato, the Taranaki basin, and the west coast of New Zealand's South Island) may be related to paleoenvironmental factors[49]. The type material is Pliocene[50], but the distinction of this species from other *Fuscospora* pollen (including *N. brachyspinulosa* and *N. waipawaensis*) is problematic. If *N. waipawaensis* and *N. senectus* are excluded, then the New Zealand FAD of other *Fuscospora* pollen would be late Paleocene.

In Southern Australia, the FAD of *N. flemingii* is in the upper part of the *Lygistepollenites balmei* Zone (late Paleocene)[51,52]. However, in a detailed study of Paleocene-Eocene transition strata in western Victoria, *N. flemingii* is not reported[53]. In New Zealand, the *N. flemingii* FAD is reported as middle Eocene[54,55]. However, in well-dated early Eocene New Zealand localities, occasional small *N. flemingii*-like specimens are observed; their identification is under debate. Due to the relative geographic proximity of East Antarctica and Southern Australia in the Paleogene, we follow [52, 53] and place the FADs of both species in the late Paleocene.

Proteacidites tenuiexinus has a range from 66.043 to 15.97 Ma (PaleoDB taxon number: 277519 at fossilworks.org). We adopt the published late Paleocene *Proteacidites tenuiexinus* FAD in Southeastern Australia[51], but acknowledge that the FAD could be as early as early Paleocene.

Two pollen species present in core JPC-54 were not observed in core JPC-55, *Nothofagidites cranwelliae* and *Nothofagidites emarcidus*. Most verified references for *Nothofagidites cranwelliae* and *Nothofagidites emarcidus* (e.g. those with specimens properly identified; the *Nothofagidites* group is diverse, complex, and easily

563 misidentified) place the FAD of both of these species in the early Eocene, at the
564 earliest[56,57]. The latter species was also found in the Eocene of Western Australia[58].
565 *Diatom preservation and biostratigraphy:* The diatom assemblages present in
566 cores JPC-30 and JPC-31 are indistinguishable, although preservation is better and
567 abundance higher in the JPC-31 diatomites compared to the sandy diatom muds
568 recovered in JPC-30. Overall, preservation is moderate to good in JPC-31 and poor to
569 moderate in JPC-30 (Extended Data Fig. 6). Diatoms in both cores suffer from a high
570 degree of fragmentation. Large centric taxa, such as *Actinocyclus* spp. and *Thalassiosira*
571 spp., are generally broken, whereas the smaller centric and pennate specimens are well
572 preserved (Extended Data Fig. 6). *Denticulopsis* specimens are generally well preserved,
573 although though the longer specimens of *D. delicata* are typically broken. *Rouxia* spp.
574 occur mostly in fragments making identification more problematic. Similarly, specimens
575 of *Fragilariopsis* spp. are dominantly present as broken specimens, with the exception of
576 a few *F. praecurta* specimens (Extended Data Fig. 6).
577 Many of the diatom species present in both JPC-30 and JPC-31 have long age
578 ranges and do not provide good biostratigraphic age constraints (e.g., *Coscinodiscus*
579 *marginatus*, *Trinacria excavata*). However, the presence of several common taxa
580 provides robust support for a late Miocene-earliest Pliocene age. These taxa include:
581 *Actinocylus ingens* var. *ovalis, Denticulopsis delicata, Fragilariopsis praecurta*,
582 *Thalassiosira oliverana* var. *sparsa, Thalassiosira torokina* (large form), and
583 silicoflagellates in the *Distephanus speculum speculum 'pseudofibula* plexus' group.
584 There is very little evidence of reworking of older material, with only one specimen of
585 *Pyxilla* sp. and a fragment of *Hemiaulus* sp. observed; all species within both of these

586 genera are typical of the Eocene and Oligocene.

587 *Age determination for JPC-55 sediments*: Based on our conservative pollen
588 zonation scheme, we favor a late Paleocene to earliest early Eocene age for the
589 exceptionally diverse JPC-55 *in situ* fossil pollen assemblage; this assemblage is easily
590 distinguishable from reworked Cretaceous microfossils present in the sediments (Fig. 2b).
591 The presence of middle bathyal benthic foraminifer species *Gyroidinoides globosus* and
592 *Palmula* sp.*,* both of which went extinct at the Paleocene-Eocene boundary[59], enables us
593 to further refine the pollen-based age designation to late Paleocene (Extended Data Fig.
594 5). Although its first occurrence may be diachronous, the presence of aragonitic Cenozoic
595 benthic foraminifer species *Hoeglundina elegans*[59-63] indicates that these sediments are
596 Cenozoic in age, confirming the interpretation that co-occurring Cretaceous microfossils
597 are reworked. *H. elegans* and other aragonitic benthic foraminifers are most common in
598 upper to middle bathyal assemblages along the southern Australian margin and the
599 Australo-Antarctic Gulf during the Paleocene and Eocene[60,63]. Thus, we conservatively
600 designate an age of late Paleocene to sediments in the lower unit (Unit 2) of JPC-55 (Fig.
601 2b, Extended Data Fig. 2b).

602 *Age determination for JPC-54 sediments:* Pollen bistratigraphy constrains the
603 depositional age of JPC-54 Unit 2 sediments to the early-to-middle Eocene (Fig. 2b,
604 Extended Data Fig. 3b). No foraminifers are observed in the lower lithologic unit of JPC-
605 54. Thus, based on the pollen assemblage alone, we favor an early-to-middle Eocene age
606 for sediments in the lower unit (Unit 2) of JPC-54.

607 *Age determination for JPC-30 and JPC-31 sediments:* Based on Southern Ocean
608 diatom ages[42], the FAD of *T. oliverana* var. *sparsa* (8.61 Ma) and the LAD of *T. ingens*

609 var. *ovalis* (4.78 Ma) provide a conservative age estimate for the diatom assemblages
610 present in JPC-30 and JPC-31 (8.61–4.78 Ma; Fig. 2d). A more restricted age
611 interpretation is possible if the presence of *Shionodiscus tetraoestrupii* (FAD 6.91 Ma)
612 and the absence of the typical early Pliocene taxon *Thalassiosira inura* (FAD 5.59 Ma)
613 are considered, indicating an age between 6.91 and 5.59 Ma (Fig 2d). This more
614 restricted age should be considered tentative, since precise calibrations for many
615 Southern Ocean diatom bioevents in the Chron C3–C3A (4.2-7.1 Ma) interval are
616 compromised by multiple short hiatuses at many drill sites and poor magnetostratigraphy.
617 Further age refinement for the JPC-30 and JPC-31 samples is likely possible as diatom
618 biostratigraphic data are published for expanded Late Neogene sections recovered on the
619 Wilkes Land margin[64]. However, the more conservative age estimate (8.61-4.78 Ma; Fig.
620 2d) is well supported by the presence of several taxa with well-calibrated ages in the
621 Southern Ocean, including *Rouxia naviculoides* (FAD 9.84 Ma), *Thalassiosira oliverana*
622 (FAD 9.73 Ma), and *Thalassiosira torokina* (FAD 9.36 Ma). The absence of
623 *Denticulopsis dimorpha* (LAD 9.75 Ma, *Denticulopsis ovata* (LAD 8.13), *Thalassiosira*
624 *complicata* (FAD 5.12 Ma), *Fragilariopsis barronii* (FAD 4.38 Ma), and *Fragilariopsis*
625 *interfrigidaria* (FAD 4.13 Ma) support this age assessment.
626
627 **Data availability.** The seismic data from the study are available in the Academic Seismic
628 Datacenter at the University of Texas Institute for Geophysics (http://www-
629 udc.ig.utexas.edu/sdc/cruise.php?cruiseIn=nbp1402). Sediment cores are archived in the
630 NSF-funded Antarctic Core Repository at Oregon State University. The authors declare
631 that all other data that support the findings of this study are available within the paper and

its supplementary information files; these data may also be downloaded from the US Antarctic Program Data Center (USAP-DC; www.usap-dc.org).

Methods References

31. Anderson, J. & Bartek, L.R. Cenozoic glacial history of the Ross Sea revealed by intermediate resolution seismic reflection data combined with drill site information. pp. 213–263 *in* The Antarctic Paleoenvironment: A Perspective on Global Change. J.P. Kennett and D.A. Warnke, eds., *Antarctic Research Series*, vol. 56, American Geophysical Union (1992).

32. Ó'Cofaigh, C. Tunnel valley genesis. *Prog. Phys. Geog.* **20**, 1-19 (1996).

33. Huuse, M. & Lykke-Andersen, H. Over-deepened Quaternary valleys in the eastern Danish North Sea: morphology and origin. *Quat. Sci. Rev*. **19**,1233-1253 (2000).

34. Denton, G.H. & Sugden, D.E. Meltwater features that suggest Miocene ice-sheet overriding of the Transantarctic Mountains in Victoria Land, Antarctica. *Geogr. Ann. A* **87**, 67-85 (2005).

35. Lonergan, L., Maidment, S. & Collier, J. Pleistocene subglacial tunnel valleys in the central North Sea basin: 3-D morphology and evolution. *J. Quat. Sci.* **21**, 891-903 (2006).

36. Elmore, C.R., Gulick, S.P.S., Willems, B., & Powell, R., Seismic stratigraphic evidence for glacial expanse during glacial maxima in the Yakutat Bay Region, Gulf of Alaska. *Geochem. Geophys. Geosys.* **14**, p. 1294-1311 (2013).

37. Van der Vegt, P., Janszen, A., & Moscariello, A. Tunnel valleys: current knowledge and future perspectives. *Geol. Soc. London Spec. Publ.* **368**, 75-97 (2012).

38. Bjarnadóttir, L.R., Winsborrow, M.C.M., & Andreassen, K. Large subglacial meltwater features in the central Barents Sea. *Geology* **45**,159-162 (2017).

39. Piotrowski, J.A. Subglacial hydrology in north-western Germany during the last glaciation: Groundwater flow, tunnel valleys and hydrologic cycles. *Quat. Sci. Rev* **16**, 169-186 (1997).

40. Bart, P.J. Were West Antarctic Ice Sheet grounding events in the Ross Sea a consequence of East Antarctic Ice Sheet expansion during the middle Miocene? *Earth Planet. Sci. Lett.* **216**, 93-107 (2003).

41. Scherer, R.P. A new method for the determination of absolute abundance of diatom and other silt-sized sedimentary particles. *J. Paleolimnology* **12**, 171-179 (1994).

42. Crampton, J.S. *et al.* Southern Ocean phytoplankton turnover in response to stepwise Antarctic cooling over the past 15 million years. *Proc. Natl. Acad. Sci. USA* 113, 6868-6873 (2016).

43. Contreras, L. *et al*. Southern high-latitude terrestrial climate change during the Paleocene–Eocene derived from a marine pollen record (ODP Site 1172, East Tasman Plateau). *Clim. Past Discuss.* **10**, 291-340 (2014).

44. Partridge, A.D. Late Cretaceous-Cenozoic palynology zonations Gippsland Basin, Australian Mesozoic and Cenozoic palynology zonations-update to the 20004 Geologic Time Scale, Geoscience Australia, Record 2006/23 (2006).

45. MacPhail, M.K.& Truswell, E.M. Palynology of Site 1166, Prydz Bay, East Antarctica. *In* Cooper, A.K., O'Brien, P.E. & Richter, C. (*Eds.*), *Proc. ODP, Sci. Results* **188**, 1-43 (2004).

46. Truswell, E.M. & MacPhail, M.K. Fossil forests on the edge of extinction: What does the fossil spore and pollen evidence from East Antarctica say? *Austral. Syst. Bot.* **22**, 57-106 (2009).

47. Raine, J.I., Mildenhall, D.C. & Kennedy, E.M. New Zealand fossil spores and pollen: an illustrated catalogue. 4th edition. GNS Science Miscellaneous Series, 4, http://data.gns.cri.nz/sporepollen/index.htm (2011).

48. Hill, R.S. (Ed.). History of the Australian vegetation: Cretaceous to Recent. Cambridge University Press (Cambridge). p. 233 (1994).

49. Truswell, E. M. Recycled Cretaceous and Tertiary pollen and spores in Antarctic marine sediments: a catalogue. *Palaeontographica Abt. B* **186**, 121-174 (1983).

50. Pocknall, D.T. Late Eocene to early Miocene vegetation and climate history of New Zealand, *J. R. Soc. N.Z.* **19**, 1-18 (1989).

51. Dettmann, M.E., Pocknall, D.T., Romero, E.J. & Zamalao, M. del C. *Nothofagidites* Erdtman ex Potonie, 1960; a catalogue of species with notes on the paleogeographic distribution of *Nothofagus* BI. (Southern Beech). *N.Z. Geol. Sur. Paleo. Bull.* **60**, 1-79 (1990).

52. Stover, L.E. & Partridge, A.D. Tertiary and Late Cretaceous spores and pollen from the Gippsland Basin, southeastern Australia. *Proc. Roy. Soc. Victoria* **85**, 237-286 (1973).

53. Stover, L.E. & Evans, P.R. Upper Cretaceous-Eocene spore-pollen zonation, offshore Gippsland Basin, Australia. *Geol. Soc. Australia Spec. Pub.* **4**, 55-72 (1973).

54. Harris, W.K. Basal Tertiary microfloras from the Princetown area, Victoria, Australia. *Palaeontographica Abt. B* **115**, 75-106 (1965).

55. Couper, R.A. New Zealand Mesozoic and Cainozoic plant microfossils. *N.Z. Geol. Sur. Paleo. Bull.* **32***,* 87 pages (1960).

56. Raine, J.I. Outline of a palynological zonation of Cretaceous to Paleogene terrestrial sediments in west coast region, South Island, New Zealand. *N.Z. Geol. Survey Rept.* **109**, 1-82 (1984).

57. Greenwood, D.R., Moss, P.T., Rowett, A.I., Vadala, A.J. & Keefe, R.L. Plant communities and climate change in southeastern Australia during the early Paleogene. *Geol. Soc. Spec. Pap.* **369**, 365-380 (2003).

58. Stover, L.E. & Partridge, A.D. Eocene spore-pollen from the Werillup Formation, Western Australia. *Palynology* **6**, 69-96 (1982).

59. Thomas, E. Late Cretaceous through Neogene deep-sea benthic foraminifers (Maud Rise, Weddell Sea, Antarctica). *Proc. ODP, Sci. Res.* **113**, 571-594 (1990).

60. McGowran, B. Two Paleocene foraminiferal faunas from the Wangerrip Group, Pebble Point Coastal section, Western Victoria. *Proc. Roy. Victoria* **79**, 9-74 (1965).

61. Brotzen, F. The Swedish Paleocene and its Foraminiferal Fauna*. Arsbok Sveriges Geologiska Undersokning*, **42**, 1-140 (1948).

62. Holbourn, A., Henderson, A. & MacLeod, N. Atlas of Benthic Foraminifera. Wiley-Blackwell, London, England. 634 pp (2013).

63. Li, Q., James, N.P. & McGowran, B. Middle and late Eocene Great Australian Bight lithobiostratigraphy and stepwise evolution of the southern Australian continental margin. *Aus. J. Earth Sci.* **50**, 113-128 (2003).

64. Tauxe, L. *et al.* Chronostratigraphic framework for the IODP Expedition 318 cores from the Wilkesland Margin: Constraints for paleoceanographic reconstruction. *Paleoceanography* **27**, PA2214, doi:10.1029/2012PA002308 (2012).

Extended Data Legends

Extended Data Figure 1| Uninterpreted NBP14-02 seismic profiles with line crossings and coring sites indicated. a, Line 13 with piston core sites JPC-30 and JPC-31 and formation penetration depths indicated by red lines. **b**, Line 17 with core sites JPC-55 and JPC-54 and formation penetration depths indicated by red lines. **c**, Line 07 showing intersection with Line 10. **d**, Line 10 showing intersections with Line 07 and Line 21. **e**, Line 21 showing intersection with Line 10.

Extended Data Figure 2| Site location and sedimentological, geochemical, and paleontological data from piston core NBP14-02 JPC-55 plotted versus depth. a, CHIRP record of JPC-55 site; location and penetration indicated (red line); site coordinates and multibeam depth (MB) included. **b**, Gastropod steinkern (70-72 cm). **c**, Siderite concretion with monocot stem nucleus (118-125 cm). **d**, Close-up of monocot stem. **e**, JPC-55 lithologic unit, photograph, x-ray radiograph, graphic lithology, coring disturbance, sedimentary structures, lithologic accessories, sample locations, age, benthic foraminifers/30 cc sediment, magnetic susceptibility, GRA bulk density (grams/cc sediment), bulk sediment $\delta^{13}C_{org}$ (per mil; VPDB‰), and Carbon/Nitrogen (C/N) plotted versus depth in in centimeters below sea floor (cmbsf; SI).

Extended Data Figure 3| Site location and sedimentological and geochemical data from piston core NBP14-02 JPC-54 plotted versus depth. a, JPC-54 lithologic unit, photograph, x-ray radiograph, graphic lithology, coring disturbance, sedimentary structures, lithologic accessories, sample locations, age, magnetic susceptibility (SI), GRA bulk density (grams/cc sediment), and bulk sediment $\delta^{13}C_{org}$ (per mil; VPDB‰) plotted versus depth in centimeters below sea floor (cmbsf). **b**, CHIRP record of JPC-54 site; location and penetration indicated (red line); site coordinates and multibeam depth (MB) included.

Extended Data Figure 4| Site location and sedimentological data from piston cores NBP14-02 JPC-30 and JPC-31 plotted versus depth. a, CHIRP record of JPC-30 site; location and penetration indicated (red line); site coordinates and multibeam depth (MB) included. **b**, JPC-30 lithologic unit, photograph, x-ray radiograph, graphic lithology, coring disturbance, sedimentary structures, lithologic accessories, sample locations, age, magnetic susceptibility (SI), and GRA bulk density (grams/cc sediment) plotted versus depth in centimeters below sea floor (cmbsf). **c**, CHIRP record of JPC-31 site; location, and penetration indicated (red line). **d**, JPC-31 lithology, age, and physical properties as above.

Extended Data Figure 5| Benthic foraminifers from piston core NBP14-02 JPC-55. **a**, *Hoeglundina elegans* (76-78 cmbsf). **b**, SEM of *Hoeglundina elegans* (76-78 cmbsf). **c**, *Ceratobulimina* sp. (70-72 cmbsf). **d**, *Ceratobulimina* sp. (70-72 cmbsf). **e**, SEM of *Ceratobulimina* sp. (70-72 cmbsf). **f**, SEM of *Gyroidinoides globosus* (110-113 cmbsf). **g**, SEM of *Gyroidinoides globosus* (110-113 cmbsf). **h**, *Gyroidinoides globosus* with pyrite (136-138 cmbsf). **i**, *Gyroidinoides globosus* with zoom in of umbilicus; pyrite on lower right side of test (136-138 cmbsf). **j**, *Palmula* sp. (136-138 cmbsf; test >450 μm).

Extended Data Figure 6| Siliceous microfossils from piston core NBP14-02 JPC-31 diatomite sample. a, *Thalassiosira torokina.* **b**, *Thalassiosira oliverana* var. *sparsa*. **c**, *Actinocyclus ingens* var. *ovalis*. **d**, *Coscinodiscus marginatus*. **e**, *Azpeitia* sp. 1. **f**, *Actinocyclus* sp. **g**, *Actinocyclus* sp. **h**, *Shionodiscus tetraoestrupii.* **i**, *Shionodiscus tetraoestrupii*. **j**, *Shionodiscus oestrupii.* **k**, *Denticulopsis delicate*. **l**, *Denticulopsis simonsenii*/*D. vulgaris.* **m**, *Denticulopsis simonsenii*/*D. vulgaris.* **n**, *Denticulopsis delicate.* **o***, Denticulopsis simonsenii*/*D. vulgaris.* **p**, *Rouxia naviculoides.* **q**, *Fragilariopsis praecurta.* **r***, Fragilariopsis* sp. 1. **s**, *Trinacria excavate.* **t**, *Rhizosolenia hebetate.* **u***, Eucampia antarctica* var. *recta*. **v**, *Distephanus speculum speculum* f. *varians*. *Sample from 43-45 cmbsf.*

Extended Data Table 1| NBP14-02 piston core locations, water depths, and recovered core lengths.

Extended Data Table 2| Piston core NBP14-02 JPC-55 and JPC-54 raw terrestrial pollen counts.

Extended Data Table 3| Piston core NBP14-02 JPC-55 raw benthic foraminifer counts.

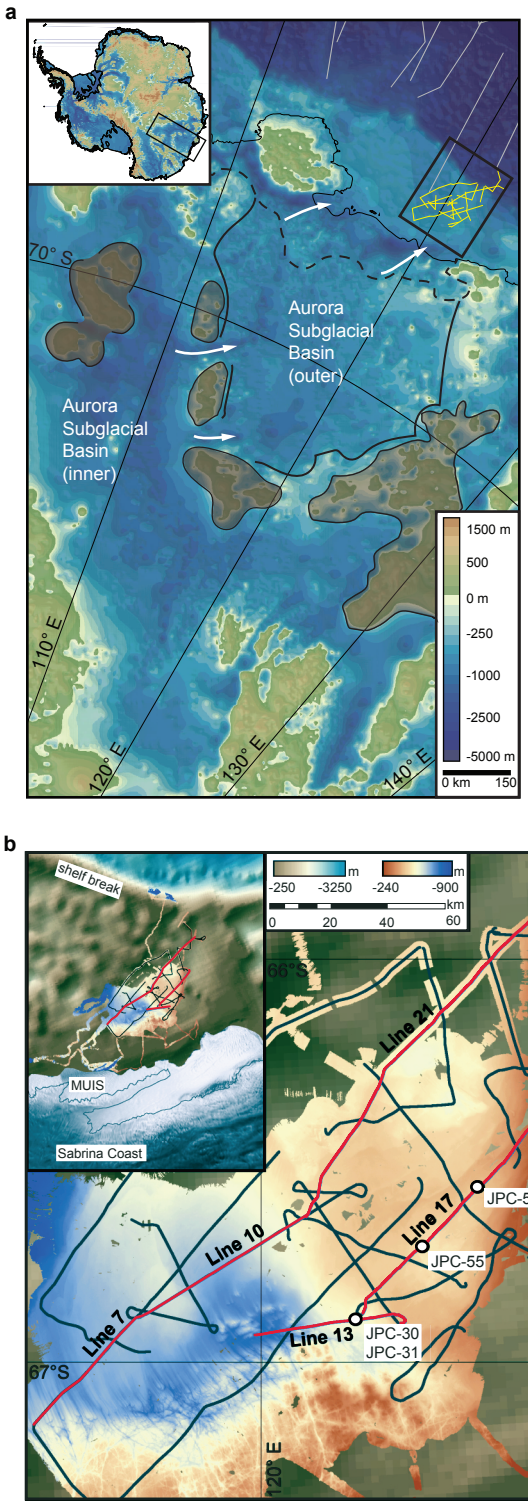

Gulick et al_Fig. 1

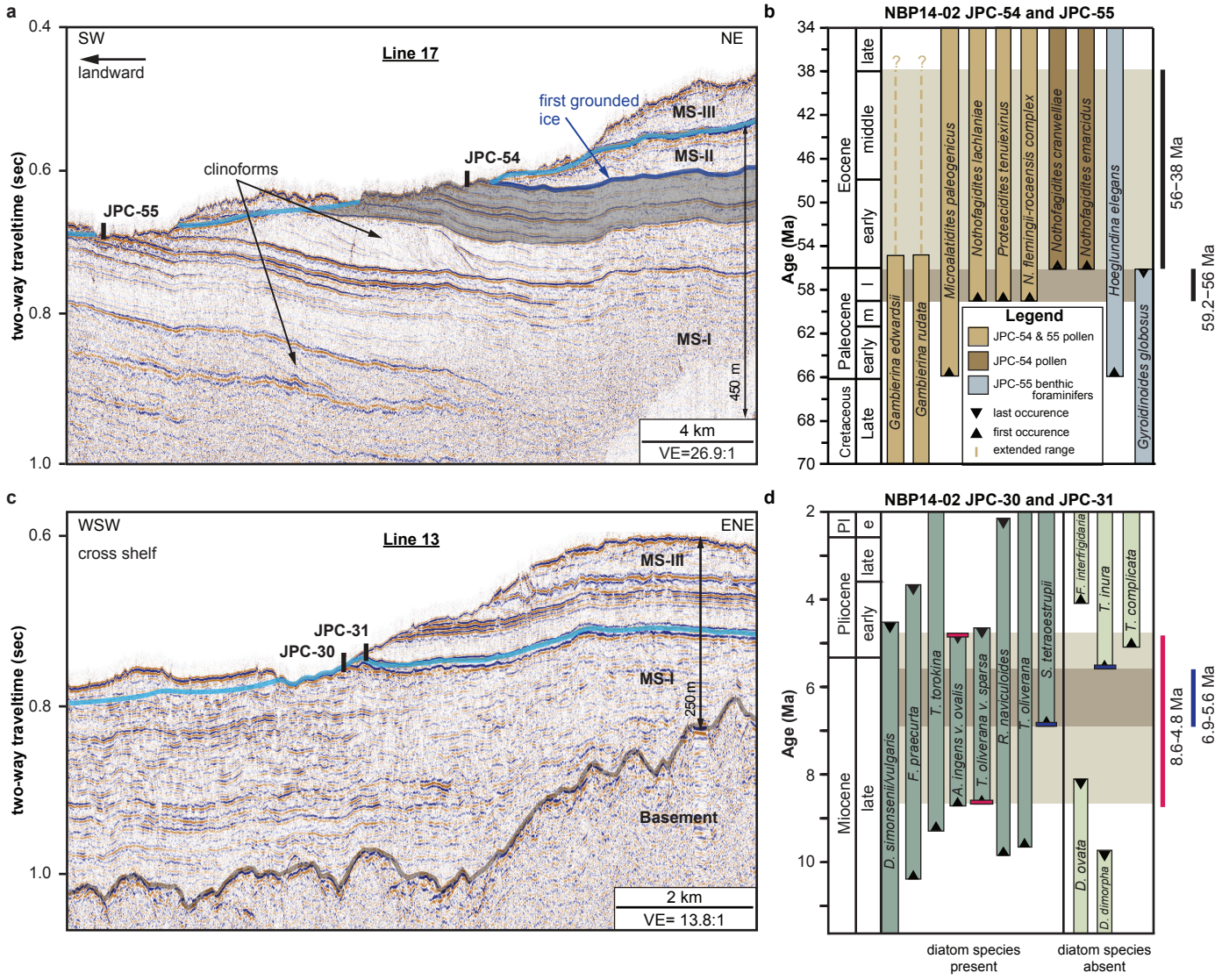

Gulick et al_Fig. 2

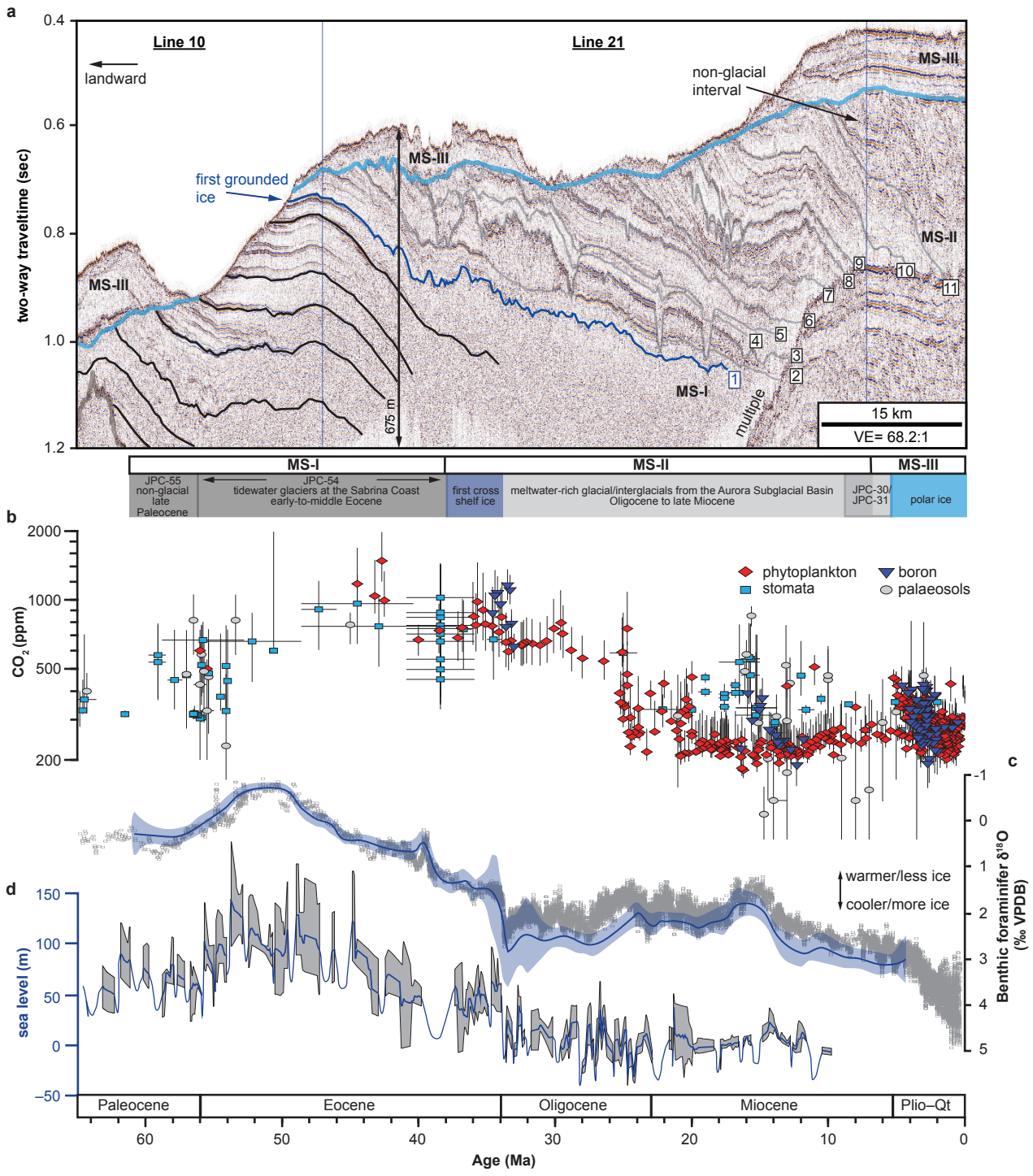

Gulick et al_Fig, 3